

Putting ultracold atoms and molecules in a box

Jochem Willem Hendricus Langen

Level 4 Project, MPhys Theoretical Physics

Supervisor: Professor S. Cornish & Dr T. Franzen

Department of Physics, Durham University

Submitted: May 30, 2023

The use of blue-detuned laser light to form box shaped traps has gained increasing interest over the years due their low light-matter interaction rate and high homogeneity. In this work, methods to generate different box traps using axicons are described and their trap parameters compared. It has been found that a trap using two 2° axicons, one 5° axicon, a single 125 mm lens and an iris generates the trap with the best parameters overall from all traps discussed. However, the overview of results given shows the best trap for any usage case of interest. A Python programme has been provided to align and characterise any box trap.

Contents

1	Introduction	3
1.1	Trapping mechanism	3
1.2	Trapping atoms	4
1.3	Trapping molecules	5
1.4	Trap parameters	5
1.5	Axicons	6
2	Single axicon trap	9
2.1	Gaussian beam	9
2.2	Axicon set-up	10
2.3	Axicon - lens set-up	12
2.4	Lens - axicon set-up	14
3	Multiple axicon trap	16
3.1	Double axicon set-up	18
3.2	Double axicons - single lens set-up	19
3.3	Iris	21
3.4	Triple axicon - single lens set-up	23
4	Results overview	25
5	Image processing	25
6	Acknowledgments	26
7	Conclusion	26
	References	26
8	Appendix	29
8.1	Camera linearity	29
8.2	Gaussian noise	29

1 INTRODUCTION

The use of lasers to trap atoms and molecules has become an integral part of modern day physics. It has many applications such as generating ultracold Bose-Einstein Condensates, trapping singular atoms with optical tweezers and generating qubits with Rydberg atoms in optical arrays [1–6]. These laser traps are often set up to form harmonic potentials. However, in recent years, interest has grown into what can be referred to as "box traps". These traps provide the opportunity to investigate homogeneous systems more directly and cause fewer light interactions, which can reduce particle losses [4–14].

This work provides an investigation into different methods to generate hollow beams using the lenses with a conical surface called axicons. These hollow beams form the basis of the box traps. In doing so, the alignment and results of each set-up is discussed. Furthermore, an image analysis programme is provided as a tool to characterise and optimise the hollow beams.

1.1 Trapping mechanism

To proceed with the investigation into particle traps, it is important to understand how the trapping mechanism works. This allows us to compare different trap types and bridge the gap between light profiles and their corresponding particle distributions.

To do so, we consider the response of an electron of a neutral atom in an electric field using the Jaynes-Cummings model [15]. The atom has a ground and excited state, $|g\rangle$ & $|e\rangle$, with energies $\mp\frac{1}{2}\hbar\omega_0$ respectively. The atom is present in a single-mode quantised light field with states $|n\rangle$ & $|n+1\rangle$ with energies $n\hbar\omega$ & $(n+1)\hbar\omega$. The electric field moves the electron, inducing a dipole moment [16], giving the interaction Hamiltonian:

$$\hat{H}_I = -\hat{\mathbf{d}} \cdot \hat{\mathbf{E}} = \hat{\mathbf{d}} \cdot \mathbf{e} g (\hat{a}^\dagger + \hat{a}), \quad (1)$$

where g depends on the phase and photon energy. Together with the free Hamiltonian for the atom, \hat{H}_A and the field, \hat{H}_F , the Jaynes-Cummings Hamiltonian is obtained in the Heisenberg picture [15]:

$$\hat{H} = \hat{H}_A + \hat{H}_F + \hat{H}_I = \frac{1}{2}\hbar\omega_0\hat{\sigma}_3 + \hbar\omega\hat{a}^\dagger\hat{a} + \hbar k (\hat{\sigma}_+ + \hat{\sigma}_-) (\hat{a}^\dagger + \hat{a}), \quad (2)$$

where \hat{a}^\dagger & \hat{a} are the creation and annihilation operators of the photon field, $\hat{\sigma}_+$, $\hat{\sigma}_-$ & $\hat{\sigma}_3$ the atomic transition and inversion operators and k the interaction coefficient, $k = \langle e | \hat{\mathbf{d}} \cdot \mathbf{e} | g \rangle g / \hbar$.

The free-field and atomic operators evolve with $e^{\pm i\omega t}$ & $e^{\pm i\omega_0 t}$ [15], which gives approximate time dependencies of the product operators from \hat{H}_I as $e^{\pm i(\omega_0 - \omega)t}$ & $e^{\pm i(\omega_0 + \omega)t}$. For light with frequencies similar to the atomic transition, the latter terms will oscillate much more quickly. This allows these terms to be averaged out, making the rotating-wave approximation [15–17], which leads to:

$$\hat{H} = \frac{1}{2}\hbar\omega_0\hat{\sigma}_3 + \hbar\omega\hat{a}^\dagger\hat{a} + \hbar k (\hat{a}\hat{\sigma}_+ + \hat{a}^\dagger\hat{\sigma}_-). \quad (3)$$

A basis of product states can be defined for this system as: $|\psi_{1n}\rangle = |e\rangle|n\rangle$ & $|\psi_{2n}\rangle = |g\rangle|n+1\rangle$ from the conservation of excitations in the system. These are the so-called bare states. In this basis, diagonalising the matrix representation for \hat{H} results in the following eigenvalues [15]:

$$E_{\pm}(n) = \left(n + \frac{1}{2}\right)\hbar\omega \pm \frac{1}{2}\hbar\Omega_n(\delta), \quad (4)$$

with $\Omega_n(\delta)$ the quantum electrodynamic Rabi frequency for $\delta = \omega_0 - \omega$, the detuning of the light. The energy term from the Rabi frequency is:

$$\frac{1}{2}\hbar\Omega_n(\delta) = \frac{1}{2}\hbar(\delta^2 + 4k^2(n+1))^{1/2} \approx \frac{\hbar\delta}{2} + \frac{\hbar k^2(n+1)}{\delta}, \quad (5)$$

where the final relation holds for $|\delta| \gg 4k^2(n+1)$, i.e. for large detuning. The 4 terms that result from this approximation give the sum of energies expected for the bare states, using the energies defined at the start of this section, with an additional term seen at the end of eq. 5. This shows that the energy of the system shifts due to its interactions, which is called the AC Stark shift. The corresponding shifted states are called the dressed states.

So, this energy shift lowers the ground state energy when the atom interacts with light, hence causing an effective potential. For the laser light used for trapping, we have a coherent photon state with average photon number \bar{n} with $\bar{n} \gg 1$ [15]. As $\bar{n} \propto I$, with I the light intensity [15], we have an effective potential due to this dipole interaction:

$$U_{dipole} = -\frac{\hbar k^2 \bar{n}}{\delta} \propto \frac{I}{\delta}. \quad (6)$$

The potential is linearly proportional to the intensity and inversely proportional to the detuning. For a red-detuned trap ($\omega < \omega_0$), the potential is negative, whilst it is positive for the opposite blue-detuned trap. For example, using a red-detuned gaussian beam creates an approximately harmonic potential with the particles trapped at the beam centre. Alternatively, using a more complex optical lay-out, a box can be created of blue-detuned walls of light which repel the particles to stay inside.

1.2 Trapping atoms

Two main applications of optical traps are found in the trapping of ultracold Bose and Fermi atomic gases. These gases provide an important experimental verification of many-body quantum systems [5–8]. Many textbook theories of these gases are based around homogeneous systems, which has required the use of methods such as local density approximations or selective probing to test these in harmonic traps [5, 6]. However, there are many phenomena for which these methods do not always suffice, such as critical phenomena with diverging correlation lengths, phases such as the Fulde-FerrellLarkin-Ovchinnikov state [5, 7–9], sound speeds in superfluids, pairing gaps in Fermi Gases or quantum depletion in Bose-Einstein Condensates [4]. The use of box traps, which has an approximately uniform potential between the walls, has therefore allowed for new discoveries, such as the Joule-Thomson effect [6].

Aside from a more uniform density distribution of the trapped gas which has allowed different research cases, a box trap has the benefit of a much lower interaction with light due to the dark centre. These interactions can otherwise cause heating of the atomic gas due to photon scattering [18]. As the scattering rate, R_{scat} follows the relation [16]:

$$R_{scat} \propto \frac{I}{\delta^2}, \quad (7)$$

The detuning, δ , can be increased to lower the scattering rate but this also decreases the size of the potential, eq. 6.

1.3 Trapping molecules

An ongoing area of research in molecule trapping regards the reduction of particle losses and the study of the molecule collisions that cause them [10–14].

Ultracold molecules have a much larger number of rovibrational states available compared to atoms. This allows many more Feshbach resonances: the collision complexes that form from these molecules sticking together [11–13]. As these complexes only break up again when the original molecules have returned to their initial absolute ground states, the complex sticking time τ_{stick} is much longer than generally seen in higher-temperature collisions [12]. For chaotic collision dynamics, τ_{stick} can be determined from Rice-Ramsperger-Kassel-Marcus theory [10–12]:

$$\tau_{stick} = \frac{2\pi\hbar\rho_s}{N_s}, \quad (8)$$

where ρ_s is the density of states of the collision complex and N_s is the number of outgoing quantum states that are energetically possible. These complexes are not bound by the trap and so their losses are determined by the distances they can travel within τ_{stick} .

The exact nature of the collision complex behaviour and their relation to the particle losses is not yet fully understood or agreed upon. However, one of the main theories is that these complexes can be excited by photons. These excitations cause them to transition to a state which does not allow them to decay back to their original molecules [10, 12]. These excited complexes therefore have increased lifetimes and cause more losses.

Due to the much lower light intensity within the trapped gas, box traps can achieve lower complex collision losses compared to harmonic optical traps with the highest intensity at the peak of the molecular gas distribution.

1.4 Trap parameters

Given the usage cases discussed above, there is a list of parameters that should be optimised to generate the most perfect trap. As the trap potential can be modelled as an isotropic power law potential [4, 6–8], the trap parameters can be extracted by fitting such potentials to images of

the trap. The power law for the intensity, I , is defined as follows:

$$I = a \cdot x^m + b, \quad (9)$$

which leads to the definitions of the parameters to optimise:

1. \bar{I}_p : the average peak intensity of the trap wall. For a given intensity of the laser beam, this characterises the efficiency of the trap.
2. \bar{m} : the average power law exponent of the potential, which defines the steepness of the wall. Steeper walls create a trap bearing more resemblance with an actual box, providing a more homogeneous potential for the area the gas is in. Furthermore, steeper walls reduce the number of particles interacting with the wall, reducing molecule losses and particle heating.
3. \bar{b}_r : the average constant in the power law fit relative to the peak intensity, characterising the darkness of the trap.
4. $\overline{\sigma_{\text{resid}}}$: the average weighted standard deviation of the residuals of the power law fit, which provides a measure of the flatness of the trap.
5. σ_i : the standard deviation on the results from power law fits taken from different angular sections of the circular profile. Here, i can denote one of the parameters above as well as the radius, R . The previous parameters provide the average over different fits. This parameter gives an additional measure of the uniformity of the trap.
6. c_- & c_+ : the linear coefficient of the trap parameters measured at different points along the axis. Taylor expanding the relation of any of the other trap parameters w.r.t. the distance along the propagation axis, the profile can be approximated to be linear for small distances to obtain a measure of the axial symmetry of the trap.

An example of the power law fit can be seen in fig. 4.

1.5 Axicons

The main component of a box trap is the hollow beam. These beams can be generated using axicons, either directly as lenses with one flat and one conical surface or through the use of Spatial Light Modulators [4, 19]. A diagram of an axicon can be seen in fig. 1. There are several ways to close these hollow beams to form the box. One way is to create two light planes to close off both ends [4, 5, 7, 8, 18, 20]. Alternatively, the hollow beam can be intersected with itself to create an oblate box [20] or it can be turned into a bottle beam using a lens to close it in on itself [20–22], see section 2.3.

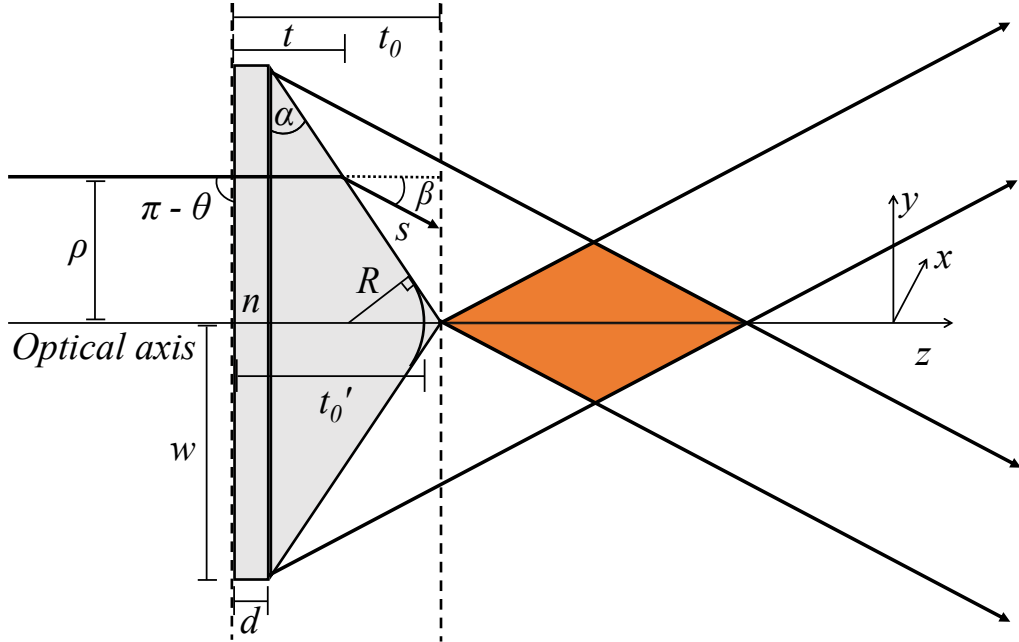


Figure 1: A diagram of an axicon and propagation of a collimated light beam. The area marked in orange shows the Bessel region.

Using geometric optics, the propagation angle of a hollow beam leaving an axicon has been derived as:

$$\beta = \arcsin \left(n \sin \left(\alpha - \arcsin \left(\frac{\sin(\theta)}{n} \right) \right) \right) - \alpha, \quad (10)$$

where θ is the propagation angle of the incoming beam, α the conical angle and n the refractive index of the axicon as can be seen in fig. 1. This propagation angle causes a collimated incoming beam to be refracted radially inward, creating a region of interference just after the axicon. The beam in this region forms an approximate zero-order Bessel beam [19–25]. Using the paraxial approximation, the length of this region, also referred to as Bessel region, is given by [21]:

$$z_{\text{Bessel}} = \frac{w}{(n-1)\alpha}, \quad (11)$$

where w is the axicon radius. For an axicon aligned in the opposite direction to what is shown in fig. 1, the propagation angle can be determined by inverting eq. 10 and relabelling β as θ and vice versa:

$$\beta = \arcsin \left(n \arcsin \left(\alpha - \arcsin \left(\frac{\sin(\theta + \alpha)}{n} \right) \right) \right). \quad (12)$$

Using the thin-lens approximation for the axicon, the imprinted phase shift, denoted as ϕ , can be derived as:

$$E_f = E_i \times e^{i\phi} = E_i \times e^{ik(t_0-t)} \times e^{iknt} = E_i \times e^{ik(1-n)\rho \tan(\alpha)} \times e^{iknt_0}, \quad (13)$$

where t_0 is the total thickness of the axicon and t the propagation length through the axicon, as displayed in fig. 1.

In reality, the tip of the axicon will not have a perfect sharp angle, which can be modelled as a spherical tip with curvature radius R . For the light with radial coordinate, ρ smaller than the tip radius, the propagation length t' has been derived as [26]:

$$t' = \sqrt{R^2 - \rho^2} - (R - t'_0), \quad (14)$$

where t'_0 is determined as:

$$t'_0 = t_0 - (R \sin(\alpha) \times \tan(\alpha) - R \times (1 - \cos(\alpha))), \quad (15)$$

which is the width of the edge and the conical surface, t_0 , subtracted by the difference in the distances between the point of the sharp perfect tip and where the rounded tip transitions and the outermost point of the arc to where the rounded tip transitions, i.e. where $\rho = R \sin(\alpha)$. The final phase shift at the rounded tip then becomes:

$$E_f = E_i \times e^{ik(1-n)(R-\sqrt{R^2-\rho^2})} \times e^{ikn t'_0} \times e^{ik(t_0-t'_0)}. \quad (16)$$

Due to the imperfect tip, neglecting the global phase, the exponentials independent of ρ , would require another approximation as it is global for the conical and circular surface individually but is not the same between the two. It has been included for that reason.

Furthermore, there is the additional effect of the refraction at the axicon-air boundary, increasing the path length for the light further away from the centre of the axicon. This path length through air, s , is changed due the diffraction by:

$$\delta s = (t_0 - t^{(\prime)}) \times \left(\frac{1}{\cos(\beta)} - 1 \right), \quad (17)$$

where β is the angle between the z-axis and the axis of propagation. For a collimated beam, eq.10 becomes:

$$\beta = \begin{cases} \sin^{-1}(n \times \sin(\alpha)) - \alpha & \text{for } \rho \geq R \sin(\alpha) \\ \sin^{-1}(n \times \sin(\sin^{-1}(|\frac{\rho}{R}|))) - \sin^{-1}(|\frac{\rho}{R}|) & \text{for } \rho < R \sin(\alpha) \end{cases}. \quad (18)$$

This effect also causes the radial coordinate of the light rays to change between the start and the end of the axicon. One way to approximate this effect is by propagating the light as geometric rays by adjusting the position of the electric field values on the grid, causing a reduction in the beam size and interference at the axicon tip. The change of position on the grid is determined by the change in the radial coordinate:

$$\delta\rho = (t_0 - t^{(\prime)}) \times \tan(\gamma). \quad (19)$$

However, if this $\delta\rho$ is big enough for this effect to be present, then the effect of the axicon could be better approximated by propagating the light through it in sections, as the thin-lens

approximation does not hold. The total phase shift, ϕ , from eq. 13 can finally thus be written as:

$$\phi = k \times \begin{cases} \left(\frac{1}{\cos(\beta)} - n \right) \rho \tan(\alpha) + n t_0 & \text{for } \rho \geq R \sin(\alpha) \\ \left(\frac{1}{\cos(\beta)} - n \right) \left(R - \sqrt{R^2 - \rho^2} \right) + n t'_0 \\ + \left(\frac{1}{\cos(\beta)} \right) \times (t_0 - t'_0) & \text{for } \rho < R \sin(\alpha) \end{cases}. \quad (20)$$

These equations have can be incorporated into the light wave simulation Python package called LightPipes [27]. The Python version of the axicon phase equations can be found here: <https://github.com/JochemLangen/trap-analysis.git>. LightPipes uses the Hedgehog propagator [26] to simulate the propagation of light waves. This programme can be used to simulate trap designs before constructing them or after to compare them, though that has fallen beyond the scope of this work.

The axicons used in the experiments discussed below are made out of UV Fused Silica. Their refractive indices, n , follow from the Sellmeier equation with the coefficients for UV Fused Silica [28]:

$$n^2 = \frac{0.6961663 \cdot \lambda^2}{\lambda^2 - 0.06840432} + \frac{0.4079426 \cdot \lambda^2}{\lambda^2 - 0.11624142} + \frac{0.8974794 \cdot \lambda^2}{\lambda^2 - 9.8961612} + 1, \quad (21)$$

where λ is the wavelength.

2 SINGLE AXICON TRAP

2.1 Gaussian beam

To generate a well predicted hollow beam with universally applicable results, the beam incident on the axicon has been made approximately Gaussian. As the shape of the Gaussian beam affects the shape of the resulting trap, it should be characterised as well.

This shape can be described by its size and divergence. From the point of collimation, the Gaussian beam slowly diverges to obtain a maximum divergence angle [26]:

$$\theta_R = \frac{\lambda}{\pi w_0}, \quad (22)$$

where w_0 is the $1/e^2$ intensity beam radius at the focus of the beam, i.e. the most collimated point. The beam diverges at this angle beyond the Rayleigh distance from the focus, given by [26]:

$$z_R = \frac{\pi w_0^2 n}{\lambda}. \quad (23)$$

The beam generated by the laser used (CPS532-C2) has been found to be notably inconsistent with a Gaussian profile, so has been filtered by coupling it into an optical fibre using a telescope. This fibre has in turn been coupled into a collimator at the other end. The resulting beam has been imaged using a CCD (CM3-U3-13Y3M-CS 1/2") with the results shown in fig. 2. Due to the concentrated high intensity area of the Gaussian beam, interference fringes appeared on the CCD caused by reflections within the camera. These have been removed by discarding the high frequency components using a Fast Fourier Transform of the original image. A 2D Gaussian fit has been performed to the resulting shape. This fit gave a value for $w_0 \approx 0.436\text{mm}$. The result can be seen in fig. 2.

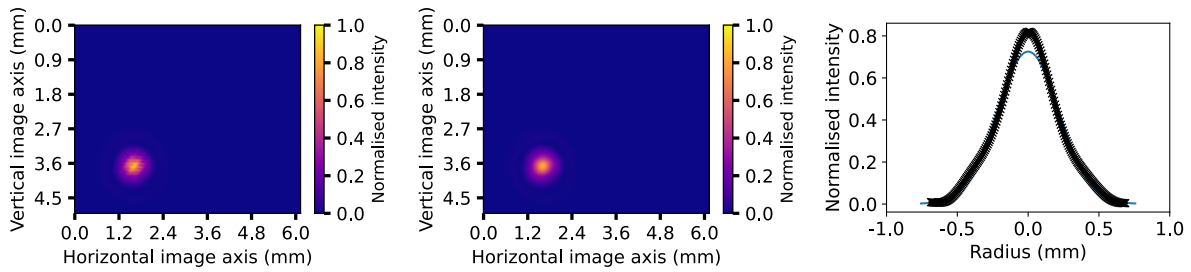


Figure 2: The Gaussian beam used for the experiment. The leftmost image shows the Gaussian beam as it appeared on the camera. The central image shows the beam with the interference fringes removed using Fourier analysis. The rightmost image shows the result from Gaussian fit (blue line) with the profile transformed onto a polar coordinate system centred around the beam peak. The points are averaged over all angles. The intensities of all these images have been normalised with the peak intensity from the original image on the left.

Using the fitted beam radius and the laser wavelength $\lambda = 532\text{nm}$, gives the following beam parameters for the beam propagating through air ($n \approx 1$): $z_R \approx 1.12\text{mm}$, $\theta_R \approx 0.0223^\circ$.

2.2 Axicon set-up

To generate a trap that is as dark as possible, it is important to minimise the amount of scattered light generated which may otherwise end up in the centre. To that end, the axicon has been placed pointing in the opposite direction to that of the light propagation. For an incoming beam concentrated by the axicon into the Bessel region, placing the axicon in such a manner reduces the total reflectivity by spreading the incident angles over all surfaces [29]. The propagation angle, β , of the hollow beam is thus given by eq. 12.

An axicon has been used with $\alpha = 5^\circ$ as the resulting β gives a scale of the experiment suitable for the optical table available. Larger α can create a more compact set-up due to larger β , however, this requires smaller focal length lenses for the set-ups described below and amplifies inaccuracies in alignment. Furthermore, these set-ups are much harder to realise when the scale is reduced to the point where certain optical elements need to be placed less than the optical

table hole spacing apart. With $\lambda = 532 \text{ nm}$, the refractive index of the axicon is $n = 1.406$, given by eq. 21.

The alignment of the axicon can be achieved by using an alignment screen or by taking images of the hollow beam. Misalignment along the xy-plane perpendicular to the propagation direction, z, causes a radial asymmetry in the intensity profile. Taylor expanding eq. 12 around $\theta = 0$, the angle of the incoming light, we find for small θ and α :

$$\beta \approx (n - 1) \cdot \alpha - \theta, \quad (24)$$

Which for $\alpha = 5^\circ$ & $\theta \pm 2^\circ$ is accurate up to 2%. This linear relation can also be seen from fig. 6. In these considerations, the angle of the beam, θ , is caused by a counterclockwise rotation of the axicon by θ , rather than the usual angle or divergence of the beam itself. The propagation angle, β , given w.r.t. the axis perpendicular to the axicon surface, has $\beta \propto -\theta$, as seen in eq. 24. So, the propagation angle w.r.t. the optical axis is obtained by shifting β with the axicon angle θ , causing the θ terms to cancel. The propagation angle is thus invariant under θ for small α & θ .

However, this change in θ causes a shift in the position of the tip in the xy-plane, r , derived as:

$$r = \tan(\theta) \cdot d_{total} = \tan(\theta) \cdot (\tan(\alpha) \cdot w + d) \approx \theta \cdot (\alpha \cdot w + d) \propto \theta, \quad (25)$$

where d_{total} is the total axicon thickness and d & w are defined in fig. 1. This gives a shift in the approximately Gaussian intensity at the tip:

$$\Delta I = I(r) - I(r = 0) = I_0 \cdot (e^{-(r)^2/w_0^2} - 1) \propto e^{-\theta^2}, \quad (26)$$

with w_0 the $1/e^2$ beam radius and I_0 the peak intensity. This means we get a change in the intensity in the ring.

The effects described above agree with what is found experimentally in the alignment process. A shift in the xy-position of the tip causes a radially asymmetric intensity of the ring as the Gaussian profile does not fall symmetrically on the axicon. As the change in the propagation angle is negligible, small positional misalignment can be adjusted for by small rotational adjustments. A kinetic mount is therefore recommended to compensate for the more inaccurate positioning of the base. The axicon can then be aligned by visually optimising the intensity profile as it appears on an alignment screen or by imaging it, where the analysis software can then be used to obtain information on radial symmetry in intensity, see section 5. The resulting hollow beam is shown in fig. 3.

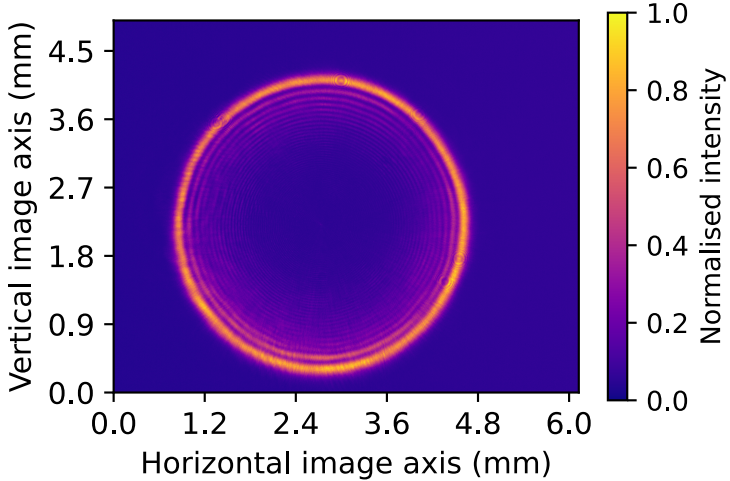


Figure 3: The hollow beam generated with a single 5° axicon. The intensity is normalised with the peak intensity of the image.

2.3 Axicon - lens set-up

To get rid of the decaying intensity light peaks going inward from the outer ring as seen in fig. 3, a lens can be placed down the optical path to focus the light onto a single ring. Aside from removing these peaks which would have made the profile unsuitable for trapping, the focusing is expected to give a higher peak intensity as well as a thinner trap wall at the focus, similar to focusing a Gaussian beam.

The lay-out of the set-up is shown in fig. 4. This depicts the additional lens with focal length f_1 to focus the ring and the lens with f_2 to image it. The f_1 lens is placed in the hollow beam region with the imaged ring at the focus of this lens. The f_1 lens is best aligned by taking the axicon back out of its post holder, after having checked the position of the lens would indeed be in the hollow beam region, and aligning it with the Gaussian beam using an alignment screen. The axicon can then be returned, now only having to align its rotation. This can be optimised by looking at the radial symmetry in the intensity by imaging the ring. Misalignment of the lens causes a shift of the ring from the propagation axis as well as a difference in the position of the focus of sections of the beam with different angles, causing radial asymmetry.

The position of the axicon along the propagation axis determines the propagation angle of the light profile around the focus. Adjusting it keeps the sum of the angles before and after the focus, describing c_- & c_+ , the same but changes the ratio between them. As a consequence, the set-up can also be used to create bottle beams when the lens is placed inside the Bessel region instead and has an appropriate value for f_1 [21]. For these bottle beams, R goes to 0 on both sides of the focus. As we are looking to create axially symmetric traps, these are not considered further.

The final ring is shown in fig. 4 and its parameters are displayed in fig. 11. The linear coef-

ficients of the trap parameters, c_- & c_+ , are determined by taking images of the ring with the f_2 lens and camera moving together on a translation stage. The set of distances used are moved through twice, with the angle of the camera slightly adjusted between them. These images have been analysed separately for their trap parameters to be combined as a weighted statistical average to then obtain the linear coefficients. This way, the error caused by the camera, coming from camera alignment, light scattering from dirt and interference within the camera, is accounted for.

For each distance and camera alignment, two images have been taken. One image has an exposure time of $52.03\ \mu s$ and one of $5000.00\ \mu s$, to capture the ring wall as well as the centre as accurately as possible. For each $5000.00\ \mu s$ image, an additional background image has been taken with the laser being blocked. During the analysis, the background image is subtracted from the each of the two images and scaled by intensity if necessary, see section . The final image which is used to extract the trap parameters from consists of a weighted average of these two images scaled to the same intensity, up to the radius where the $5000.00\ \mu s$ image first saturates, reduced by a 5% safety factor. All images throughout this work have been taken with a 0% black level, 0 dB gain and an exposure compensation of -0.06 EV.

To determine the relative peak intensity, \bar{I}_p , the average intensity of the peak of the ring was first normalised for the mean intensity in the image to obtain an intensity independent of the exposure time used. It has subsequently been multiplied by the ratio of power between the image plane and the collimator tip to account for losses in the set-up. Finally, \bar{I}_p is divided by the peak intensity of the initial beam, which was similarly normalised for the mean image intensity. For further information on the image processing, see section 5.

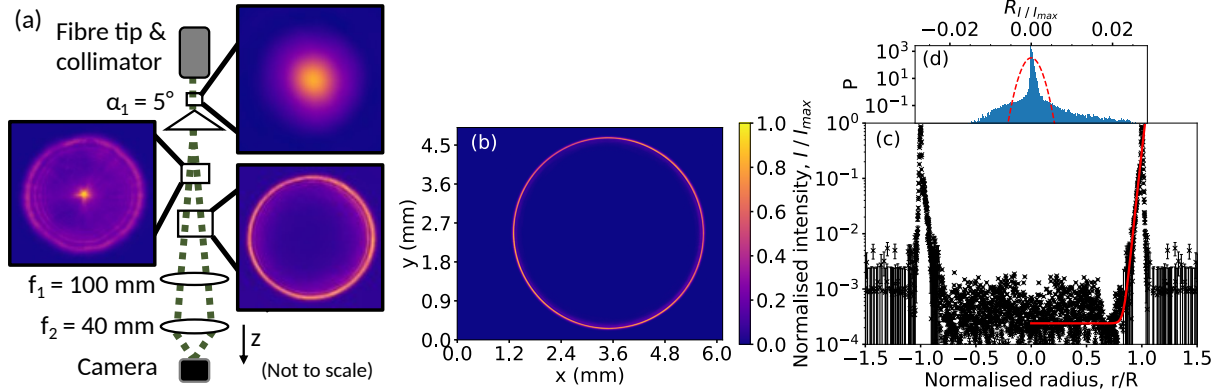


Figure 4: (a) The set-up described in section 2.3, showing the shape of the light profile through the set-up as well as the optics used. (b) The profile measured by the camera in set-up (a) as a slice in the xy -plane, perpendicular to the axis of propagation, z . (c) A slice of the profile in (b) along the radial position of all pixels with angle ϕ within error. ϕ is the angle in the polar coordinate system centred around the ring centre. The red line shows the power law fitted on the weighted mean pixel intensities in the area with $\Delta\phi = 30^\circ$ around ϕ . The intensities in (b) and (c) are normalised by the peak intensity in (b). (d) The weighted probability density of residuals around the power law fit in (c). The bins are set by the Freedman-Diaconis rule [30]. The red dashed line shows a Gaussian distribution with the standard deviation obtained from the weighted residuals.

In fig. 4 (c), the power law from eq. 9, can be seen to describe the profile up to $I \approx 2 \cdot 10^{-1}$ after which the exponent suddenly changes to become much higher. The trap wall then obtains a steepness similar to the outside of the trap. This is different from any of the other traps discussed below, where the exponent just goes to zero at the top, rather than increasing first. As the area at the bottom of the wall is what most atoms will interact with and the steepness being most crucial here, this is the area focused on.

The weighted distribution of residuals around the power law fit in fig. 4 (d) can be seen to deviate considerably from a Gaussian, consisting of a sharp peak and a wide low probability density base. The presence of these 2 sections can be explained by the relatively small number of pixels in the wall, which can have a relatively large deviation compared to the larger number of pixels in the centre. However, the shape can also indicate structure from scattered light and is thus not necessarily dominated by Gaussian noise. Furthermore, the shape is affected by the sampling of the light into 12-bit intensities, at multiple scales, and averaging over a sixth of the ring. The latter means that the small scale deviations of the trap parameters within the averaged area are all absorbed into flatness parameter. Additionally, the truncation at $I = 0$ when removing the background can cause an additional asymmetry. For more information on the Gaussian noise, see section 8.2.

2.4 Lens - axicon set-up

As described in section 2.3, moving the axicon changes the shape of the beam around the focus. However, it does not change the scale of the system. Moreover, the position of the lens can be changed to change the size of the ring that is focussed but this also changes the location of the image plane. To obtain a trap with variable dimensions, the axicon and lens need to be swapped, where the axicon position can then be varied to change the trap size.

This set-up is similar to that described in *Manek et al.* [18] and is shown in fig. 5. The axicon is placed before the focus of the lens, with the radius of the ring at the focus, R , given by [18]:

$$R = 2\alpha(n - 1) \cdot D, \quad (27)$$

where D is the distance from the axicon to the focus. This equation is valid for $f_1 = 100\text{ mm}$ and assumes $\alpha \ll 1\text{ rad} \approx 28^\circ$.

To align the system, the lens can best be aligned first using the Gaussian beam and an alignment screen. The axicon can consequently be aligned by optimising the radial symmetry of the intensity profile at or behind the focus. With the beam diverging behind the focus, there will be a point where the ring size is large enough to optimise it by eye. However, the best method to check whether both the lens and axicon are optimised correctly is by imaging the Bessel beam shown in the set-up in fig. 4. If the position of the intense peak is off-centre then the lens should be adjusted. With the imaging system on a translation stage, different sections can be imaged

to see the rings around this point moving in and out of the centre. Ensuring the movement of these rings is symmetric allows for the most accurate way to ensure the lens is optimised. Additionally, an intensity asymmetry in the rings requires adjustment of the axicon. Once the lens has been optimised, the axicon can alternatively be aligned by imaging the hollow beam and using the analysis software to extract information on the radial symmetry of the peak intensity, see section 5.

For this set-up, images with 9 different intensities, ranging from $395.77 \mu\text{s}$ to $5000.00 \mu\text{s}$, have been scaled and combined to maintain accuracy across intensity ranges. As the scattered light forms structure and the images are combined using a weighted fit, the effect of averaging out the residuals has been found to be negligible. Using this method, any points that were observed to have a lower intensity than the background due to noise, which have thus been truncated, are averaged out due to their large errors, giving a more accurate result. As no background images had been taken for this set-up, the background was instead taken as an interpolation between pixels far away enough from the profile to be approximately the same as the background.

The resulting trap and its parameters are shown in fig. 5 and fig. 11. Compared to the set-up in section 2.3, the parameters are changed by the following factors: 0.49 ± 0.05 for \bar{m} , 12 ± 6 for \bar{b}_r , 0.228 ± 0.010 for \bar{I}_p and 5.1 ± 1.3 for $\overline{\sigma_{resid}}$. This set-up thus creates a trap with less steep walls, a brighter centre, lower efficiency and lower uniformity. The radial symmetry varies, being around unity within error for all factors except for R , where σ_R is 7 ± 2 times as high. The residuals can be seen to have a notably different distribution, with a larger asymmetry and different general shape. This may be explained by the larger contribution of structure in the residuals due to the light scattering, which can be seen in fig. 5 as well as the larger value for $\overline{\sigma_{resid}}$.

The higher relative darkness and worse flatness may be accounted for using an obstructing disc. This disc can be placed at the focus to block the light in the centre, as shown in fig. 5 (a). This disc has been made using a small manufactured aluminium disc which has been glued onto a microscope slide and attached to a post.

It was found however, that it can be difficult to make a disc with a perfect shape and place it on a surface that causes negligible light scattering, which caused a varied range of parameter changes, see fig. 11. The scattering causes \bar{I}_p to be 0.66 ± 0.04 times lower. With the scattered light that then ends up in the centre, the relative darkness is 8.1 ± 0.5 times higher. As the radial asymmetry did not increase as much, σ_{b_r} is 0.28 ± 0.13 times lower but $\overline{\sigma_{Resid}}$ increased 1.3 ± 0.4 times. Additionally, \bar{m} increased 1.55 ± 0.22 times. This may be explained by a misalignment of the disc, or alternatively a disc radius that is too large, blocking out part of the wall. This would give a steeper wall but a lower efficiency and increases diffracted light in the centre if the disc is not placed exactly on the image plane. An obstructing disc may be constructed to reduce \bar{b}_r as well as $\overline{\sigma_{Resid}}$, however, its optimisation will need to be investigated further to be able to do so.

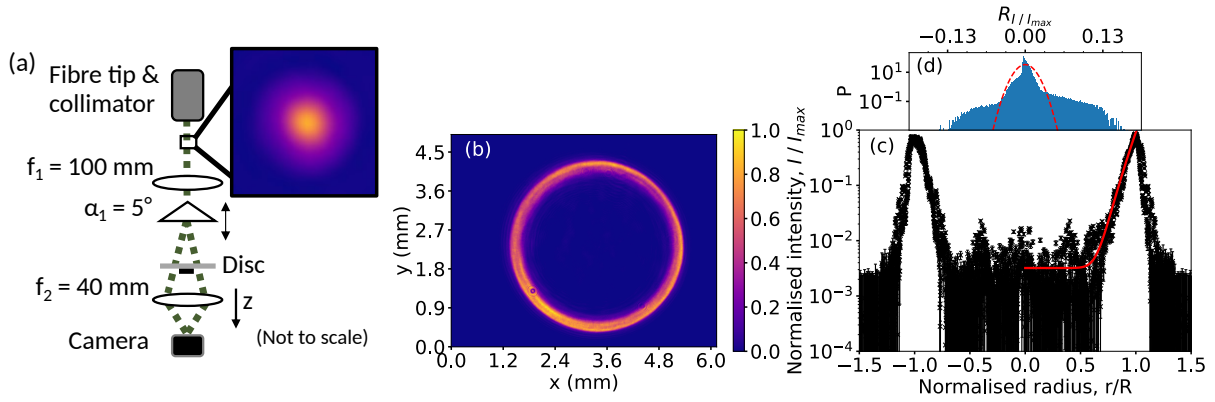


Figure 5: (a) The set-up described in section 2.4, showing the shape of the light profile through the set-up as well as the optics used. (b) The profile measured by the camera in set-up (a), though without the disc, as a slice in the xy -plane, perpendicular to the axis of propagation, z . (c) A slice of the profile in (b) along the radial position of all pixels with angle ϕ within error. ϕ is the angle in the polar coordinate system centred around the ring centre. The red line shows the power law fitted on the weighted mean pixel intensities in the area with $\Delta\phi = 30^\circ$ around ϕ . The intensities in (b) and (c) are normalised by the peak intensity in (b). (d) The weighted probability density of residuals around the power law fit in (c). The bins are set by the Freedman-Diaconis rule [30]. The red dashed line shows a Gaussian distribution with the standard deviation obtained from the weighted residuals.

The disc sets a lower limit on the size of the ring that can be varied. It can be chosen to be slightly smaller than the ring, retaining the ability for small variations, however this would come at the cost of how well the disc is optimised to block out all the central light. It was found that this limit can be reduced when moving the disc together with the axicon but this puts the disc out of the image plane and introduces diffracted light.

3 MULTIPLE AXICON TRAP

As can be seen in fig. 4, the intensity profile generated with a single axicon is generally steeper on the outside than on the inside of the ring. Inverting this profile may thus provide a better trap. This can be achieved by adding another axicon down the optical path with a conical angle that is larger than that of the first axicon. Aside from the trap wall, flipping the ring also transfers the light on the inside to the outside of the ring and vice versa. As the residual light on the inside is often caused by imperfections of the axicon tip [7], flipping the ring with an extra axicon, where none of the actual profile is incident on the tip, should reduce the amount of scattered light in the centre. This may therefore provide an alternative to an obstructing object that allows for more variable ring sizes.

Additionally, a beam created with just a single axicon cannot be fully collimated with lenses due to the linear phase it imprints [5]. This can be achieved however when using multiple axicons. With two axicons, the ring generated with the first axicon can be collimated; whereas with three axicons, it can be flipped as well as collimated.

To choose the right axicons and position them correctly, it is useful to determine the propagation angles, β , of the different beams. The propagation angle out of the 2nd axicon, β_2 , is found by taking the propagation angle of the first axicon, β_1 , as the incoming angle in eq. 10 & 12 and a subsequent sign change. This change comes from the light propagating out of the top/bottom of the first axicon then refracting in the bottom/top of the second. If derived directly, one would find a sign change in front of both the incoming and conical angles, which equates to the same result. This process can be repeated to obtain the propagation angle out of the third axicon.

Fig. 6, shows that deviations in β from the two orientations of the 2nd axicon, described by eq. 10 & 12 are amplified for larger conical angles of both the 1st (α_1) and 2nd axicon (α_2) as well as the incident angle of the incoming beam, θ . Furthermore, with the 1st axicon pointing against the direction of propagation, neither orientation of the 2nd axicon give a perfectly collimated beam. However, this is closer for the 2nd pointing opposite to the 1st. Nevertheless, for a collimated beam and an α_1 of 2° , this deviation is in the order of arcseconds, where the validity of these equations may be questioned.

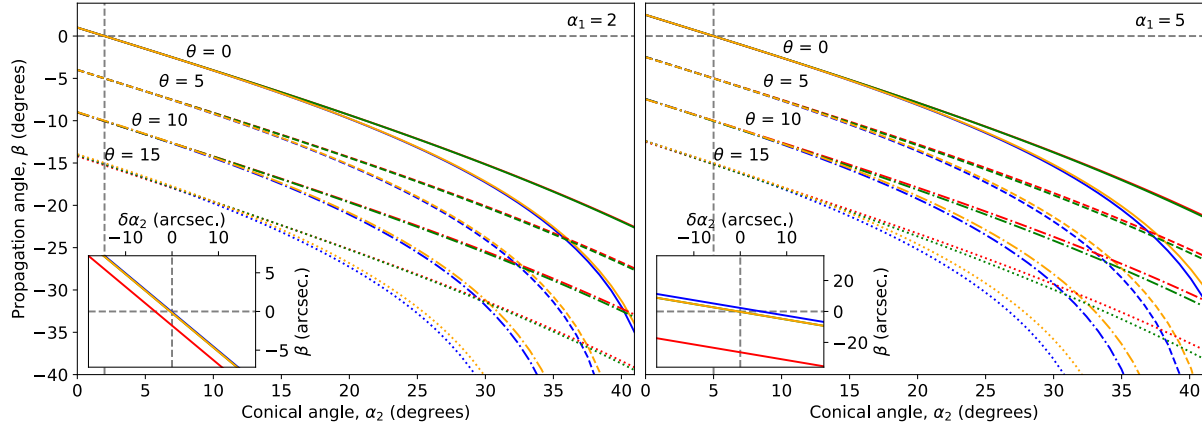


Figure 6: The differences in the final propagation angle, β , of a 2 axicon system for different orientations of the 2nd axicon, conical angles, α , and incoming propagation angles, θ . The red and blue lines describe axicons pointing against and along the propagation direction respectively. The green and the yellow lines describe β calculated from a combined axicon angle (eq. 28), pointing against and along the propagation direction respectively. The subplots display β for a small variation in α_2 : $\alpha_2 - \alpha_1$, the conical angles of the 2nd and 1st axicon. The vertical grey dashed lines mark the values of α_1 and the horizontal lines mark $\beta = 0$. The 1st axicon points against the direction of propagation.

As the phase imprinted by an axicon is linear and proportional to the tangent of the axicon angle (eq. 13), placing two axicons right after one-another to form an approximately thin system gives a combined phase that is proportional to the sum of the tangents of the angles. These two

axicons can then be replaced by a single axicon with an effective conical angle:

$$\alpha_{eff} = \tan^{-1} (\tan(\alpha_1) \pm \tan(\alpha_2)) \approx \alpha_1 \pm \alpha_2. \quad (28)$$

The sign in the sum depends on whether the 2nd axicon is convex, as has been used before, or concave. The resulting β from substituting α_{eff} into eq. 10 & 12 has been found to be very similar to that found by calculating β_2 from β_1 as described previously, which is shown in fig. 6. For this purpose, the negative sign inside eq. 28 can be used to describe the 2nd axicon being placed in the hollow beam region, so with an inverted (x,y) position of the light profile rather than an inverted axicon. The deviation between the two orientations of the 2nd axicon can be seen to be smaller using this approximation, causing the accuracy of it to degrade when the deviations between eq. eq. 10 & 12 are amplified. The approximation at the end of eq. 28 is not shown in fig. 6 but amplifies the inaccuracy at large α . It can be used as a estimate of the propagation angle when axicons with α in the order of several degrees are used with a collimated beam.

3.1 Double axicon set-up

This set-up investigates the feasibility of using two axicons without lenses to generate a trap. As the concentric rings made the single axicon set-up unusable, see section 2.2, a 2nd axicon to put these on the outside would seem to give a suitable trap.

For this set-up, $\alpha_2 = 5^\circ$ and $\alpha_1 = 2^\circ$, which has been chosen to be able to flip the beam and retain an α_{total} in the same order of magnitude as α_1 . This creates a hollow beam with a similar scale as used section 2. Both axicons have been set up to point against the direction of propagation to minimise the scattered light as discussed in section 2.2.

After having aligned the first axicon (see section 2.2), the alignment of the second determines the shape of the profile rather than the intensity distribution along it and is placed in the hollow beam region. Misalignment of this axicon causes a distorted circle, with a cusp on the edge along the misaligned axis. Further misalignment turns this cusp into a ring itself inside the main ring, which can end up creating an ∞ sign. This axicon can be aligned by visually optimising the ring shape in the far-field or by investigating it through imaging. The use of images will likely provide a more precise optimisation through visual investigation or the processing software which can be used to extract information on ring symmetry, see section 5.

Similar to section 2.3, images were taken at a set of distances for 2 camera configurations. At each distance and configuration, 4 images were taken with intensities ranging from $1499.95 \mu s$ to $13177.04 \mu s$ as well as one background image at the highest intensity. The set-up and the resulting ring can be seen in fig. 7 and the corresponding parameters are plotted in fig. 11.

The linear coefficients in fig. 11 give a propagation angle: $\beta = 1.711 \pm 0.008^\circ$. Using the geometric optics described previously, we find $\beta = 1.388$ for a perfectly collimated beam. The

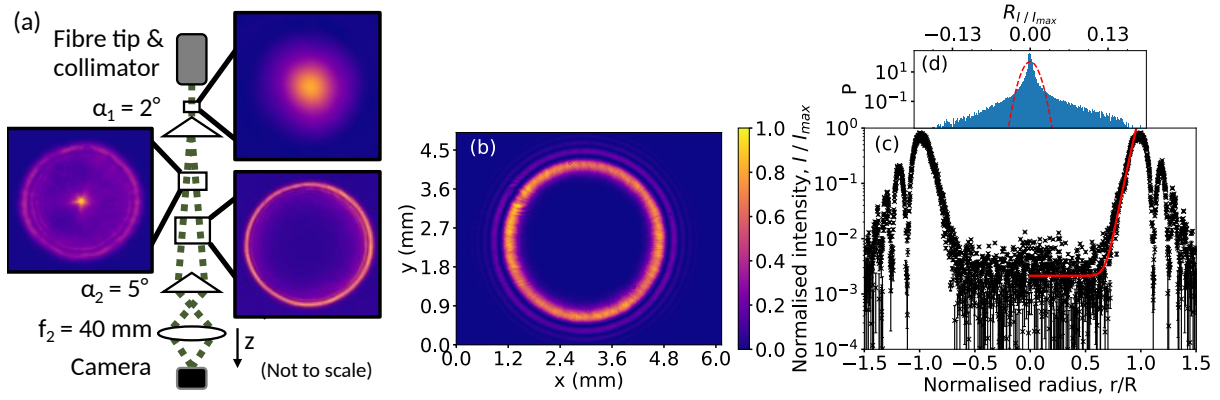


Figure 7: (a) The set-up described in section 3.1, showing the shape of the light profile through the set-up as well as the optics used. (b) The profile measured by the camera in set-up (a) as a slice in the xy-plane, perpendicular to the axis of propagation, z. (c) A slice of the profile in (b) along the radial position of all pixels with angle ϕ within error. ϕ is the angle in the polar coordinate system centred around the ring centre. The red line shows the power law fitted on the weighted mean pixel intensities in the area with $\Delta\phi = 30^\circ$ around ϕ . The intensities in (b) and (c) are normalised by the peak intensity in (b). (d) The weighted probability density of residuals around the power law fit in (c). The bins are set by the Freedman-Diaconis rule [30]. The red dashed line shows a Gaussian distribution with the standard deviation obtained from the weighted residuals.

inconsistency between these results implies the incoming beam is slightly diverging. The angle of divergence that would satisfy the data is: $\theta = 0.00565 \pm 0.00015^\circ$. This is less than the maximum divergence of the beam beyond the Rayleigh length and therefore not inconsistent with theory as the first axicon is placed $\approx \frac{1}{4} \times z_R$ away from the collimator, see section 2.1.

From fig. 7, the additional rings can now be seen on the outside, however, the inversion has also widened the bright ring. Compared to the Axicon - lens trap, this causes the trap parameters to be different with a factor of: 0.496 ± 0.002 for \bar{m} , 11 ± 6 for \bar{b}_r , 0.195 ± 0.003 for \bar{I}_p and 3.2 ± 0.7 for σ_{resid} . Furthermore, the radius of the ring is also less symmetric, with the relative std. σ_R being 2.4 ± 0.4 times higher. However, this relative radial symmetry is better for all other trap parameters, reducing by factors of 0.51 ± 0.03 for σ_m up to 0.29 ± 0.16 for σ_{b_r} . The differences in radial symmetries show the different effects of alignment imperfections between a lens and a second axicon.

The lens in the Axicon - lens set-up gives a phase opposite to the axicon, making the final beam more axially symmetric. However, the double axicon set-up has a smaller effective axicon angle $\alpha_{\text{eff}} \approx 3^\circ$. Nevertheless, the average linear coefficient in R is 2.32 ± 0.03 times higher, although this trend is not seen for all parameters, see fig. 11.

3.2 Double axicons - single lens set-up

In the previous section, the double axicon set-up has been found to generally have worse trap parameters. For that reason, instead of just adding an additional axicon to obtain a more colli-

mated beam, improving the ring itself is considered first. This can be done using an additional lens to focus the outer rings onto the inner ring as well as decreasing its width, similar to the single axicon case in section 2.3. This is expected to improve efficiency and create steeper and higher walls, reducing the relative darkness and increasing the relative flatness.

This set-up can be aligned starting from the double axicon set-up and adding the lens or the axicon - lens set-up and adding the 2nd axicon. In both cases, the optical element to be added mainly adjusts the shape of the ring and can therefore be aligned well by optimising the symmetry of the Bessel beam. Similar to the single axicon case in section 2.4, the Bessel region just after the 2nd axicon can be imaged to centre the bright spot in the middle of the rings. A translation stage can be a useful tool to see the rings move in and out of the bright spot by moving the image plane back and forward, fine-tuning the optimisation. Misalignment of the lens creates an asymmetry in the beam parameters, moving the position of the peak intensity to different radii along the ring or causing certain sections of the ring to be out of focus whilst others are. Misalignment of the axicon again distorts the radial symmetry of the ring radius.

As discussed previously, the second axicon flipped the residual light on the inside of the ring to the outside and vice versa. Instead of blocking residual light by an obstructing disc, the inversion of the light profile allows the use of an iris to block out the light around the ring before inverting it. To this end, an iris is placed just before the Bessel region of the second axicon, see section 3.3.

For each distance, two camera configurations were used each with 3 exposure times ranging from $499.96 \mu\text{s}$ to $13177.04 \mu\text{s}$ and background images taken for the highest exposure. The set-up and profile is shown in fig. 8 with the trap parameters displayed in fig. 11.

Compared to the double axicon set-up, most trap parameters have improved as predicted. The broad trap wall in fig. 7 has been focused to form the steeper wall seen in fig. 8. The trap parameters have changed by the following factors: 5.21 ± 0.07 for \bar{m} , 0.187 ± 0.014 for \bar{b}_r , 2.91 ± 0.05 for \bar{I}_p and 0.19 ± 0.02 for $\bar{\sigma}_{resid}$. The relative radial symmetry has improved for R , \bar{b}_r & $\bar{\sigma}_{resid}$ by slightly less than unity but is 1.46 ± 0.08 & 3.45 ± 0.11 times worse for \bar{m} & \bar{I}_p respectively. Furthermore, the axial symmetry has generally increased for all parameters, changing with a factor of 1.701 ± 0.015 for R . This is to be expected as the lens refracts the light in the same direction as the second axicon, increasing β . To improve the collimation, an additional axicon can be added, see section 3.4.

When comparing the double axicon - lens set-up with the axicon - lens set-up, it can be seen from fig. 11 that \bar{m} improves by a factor of 2.58 ± 0.04 , hence creating the steeper wall on the inside as desired. However, the efficiency is only 0.566 ± 0.008 times that of the axicon - lens set-up, which consequently increases the relative darkness by 2.0 ± 1.1 , due to having a similar absolute darkness, being just 15% higher. In contrast, the relative residuals have reduced, creating a flatter trap with a reduction factor of 0.60 ± 0.12 in $\bar{\sigma}_{resid}$.

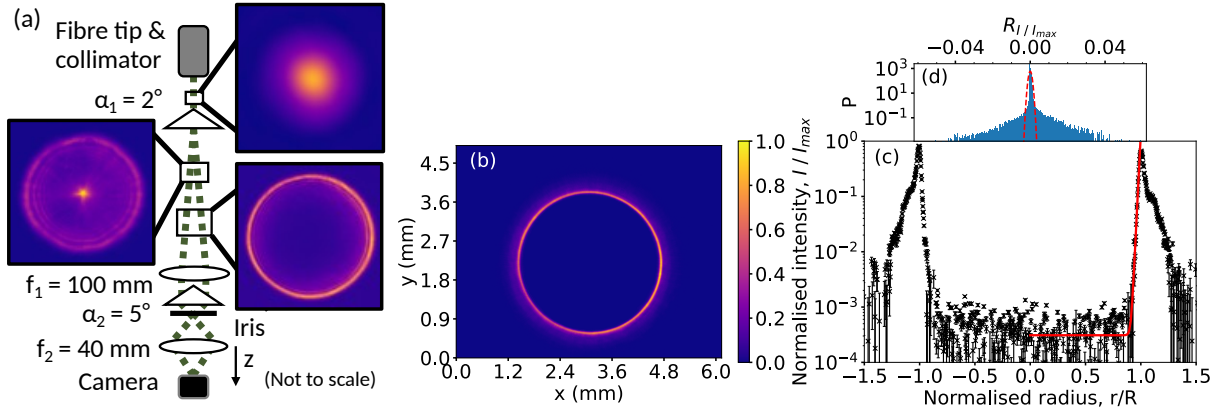


Figure 8: (a) The set-up described in section 3.2, showing the shape of the light profile through the set-up as well as the optics used. (b) The profile measured by the camera in set-up (a) as a slice in the xy-plane, perpendicular to the axis of propagation, z. (c) A slice of the profile in (b) along the radial position of all pixels with angle ϕ within error. ϕ is the angle in the polar coordinate system centred around the ring centre. The red line shows the power law fitted on the weighted mean pixel intensities in the area with $\Delta\phi = 30^\circ$ around ϕ . The intensities in (b) and (c) are normalised by the peak intensity in (b). (d) The weighted probability density of residuals around the power law fit in (c). The bins are set by the Freedman-Diaconis rule [30]. The red dashed line shows a Gaussian distribution with the standard deviation obtained from the weighted residuals.

3.3 Iris

One of the reasons to invert the ring profile with a second axicon is to remove the residual light in the centre, which is expected to be higher than on the outside of the ring [7]. Nevertheless, the area on the outside that is flipped inwards can still retain levels of scattered light that could be removed. This can be achieved using an iris, placed just before the ring inversion, i.e. the 2nd Bessel region.

Compared to an obstructing disc, the iris has the benefit of not adding an additional transmitting surface which can cause refraction and light scattering. Furthermore, they tend to be easily adjustable, in contrast to the discs, which allows the iris to be re-used for fully different or adjusted set-ups. Additionally, the element that allows for ring variability in the flipped set-up is placed after the iris, which means it does not even have to be adjusted for different ring sizes, see section 3.4.

The alignment of the iris has been investigated in the set-up shown in fig. 8. For each iris radius, 3 images were taken at 3 set exposure times ranging from $499.96 \mu\text{s}$ to $13177.04 \mu\text{s}$. The order of the radii investigated was varied to account for any time dependent variations in the final alignment profile in the parameters. Two background images were taken at each exposure time, one before and one after all the data was taken. However, due to the time variation in the background that had later been observed, the background extrapolation method was used instead as a more accurate background estimate.

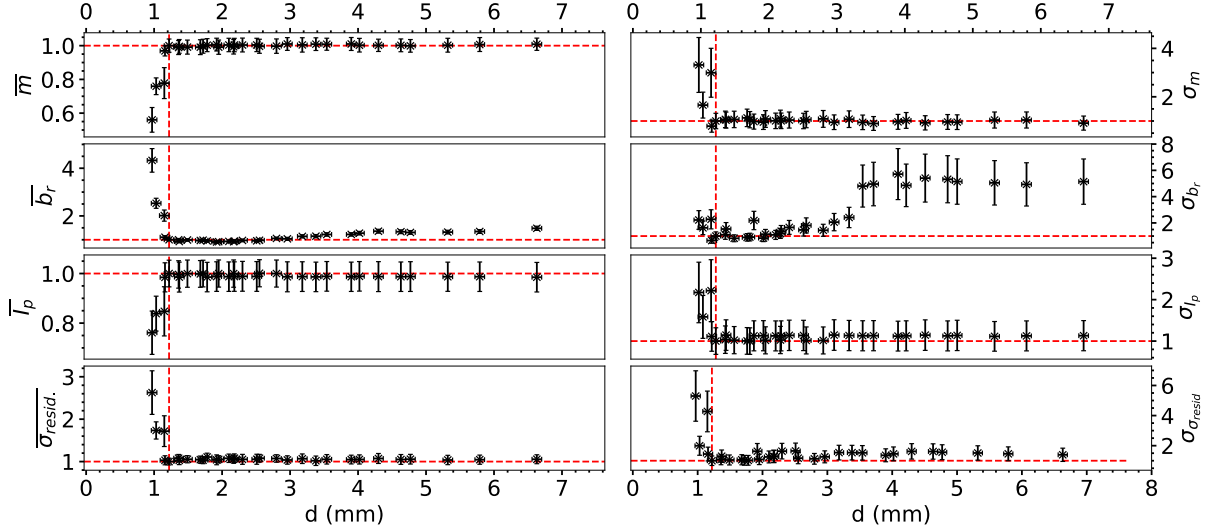


Figure 9: The variation of normalised trap parameters, which are defined in fig. 11, with iris diameter d . The parameters are normalised by their values at the measured optimum iris diameter: $d = 1.22 \pm 0.05 \text{ mm}$. The optimum values are marked with the red dashed lines.

The relative variation of trap parameters with iris diameter is shown in fig. 9. It can be seen that reducing the iris diameter towards its optimum position reduces the relative background and its radial symmetry. In particular, a transition in \bar{b}_r and σ_{b_r} can be seen between 3.5 & 4.5 mm, above which these parameters do not show a linear trend. This can indicate the limit of the light that has inverted into the centre of the ring at the image plane. Alternatively, as the axicon has a radius of 6.35 mm, the measured transition can indicate the imprint of the axicon radius further down the propagation axis.

At the transition diameter, the darkness and its symmetry can be seen to improve quickly, followed by a slower improvement up to the optimum position. This indicates that most of the residual light in this case comes from further away from the ring. The flatness can be seen to improve as well, in particular the radial symmetry of the flatness, though less so than the relative darkness. The residual light removed with the iris therefore contains some structure from scattered light but mostly consists of a uniform background.

As the intensity is determined relative to the mean image intensity, blocking out residual light generates a slight improvement in I_p , though this is corrected for with the associated power of these images in the results in fig. 11. All trap parameters display a clear diameter under which they rapidly get worse, indicating that the iris has started blocking out part of the trap wall, reducing the peak intensity and wall steepness whilst introducing scattered light.

3.4 Triple axicon - single lens set-up

The double axicon - lens set-up in section 3.2, had the drawback of low axial symmetry in its radius. This can be remedied by the introduction of a third axicon to collimate the light. Furthermore, the position of this axicon can be used to vary the final ring size as is done in *Hueck et al.* [7].

A 3rd axicon with $\alpha_3 = 2^\circ$ has been chosen to add up to an α_{eff} as close to zero as possible, see eq. 28, subject to axicon availability. The axicon is placed after the 2nd Bessel region and points towards the propagation direction to reduce light scattering as discussed in sections 2.2 & 3.1. Placing the axicon closer to this region results in a smaller final ring due to a smaller ring being collimated. As the beam is close to being collimated, there is no additional Bessel region, within reasonable distance or at all depending on the optics used, that can be utilised for alignment. Instead, the beam can be aligned using images alongside the analysis software to extract parameters on radial symmetry. Similar to the 2nd axicon, the position of the 3rd axicon determines the shape of the final profile.

Images have been taken for a range of distances with the camera at 2 slightly different angles as before. For each configuration, images were taken for 3 exposure times ranging from 499.96 μs to 13177.04 μs . Background images were taken at 13177.04 μs . The set-up and its results can be seen in fig. 10 & 11.

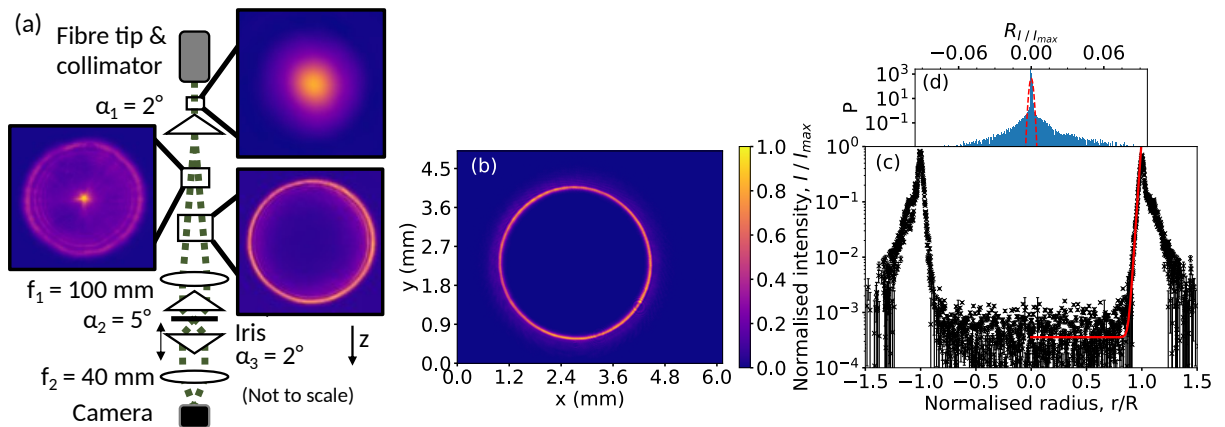


Figure 10: (a) The set-up described in section 3.4, showing the shape of the light profile through the set-up as well as the optics used. (b) The profile measured by the camera in set-up (a) as a slice in the xy -plane, perpendicular to the axis of propagation, z . (c) A slice of the profile in (b) along the radial position of all pixels with angle ϕ within error. ϕ is the angle in the polar coordinate system centred around the ring centre. The red line shows the power law fitted on the weighted mean pixel intensities in the area with $\Delta\phi = 30^\circ$ around ϕ . The intensities in (b) and (c) are normalised by the peak intensity in (b). (d) The weighted probability density of residuals around the power law fit in (c). The bins are set by the Freedman-Diaconis rule [30]. The red dashed line shows a Gaussian distribution with the standard deviation obtained from the weighted residuals.

The shape of the profile as seen in fig. 8 can be seen to be retained in fig. 10. However, the additional optical element has introduced additional losses and scattered light, which has changed the parameters by the following factors: 0.629 ± 0.014 for \bar{m} , 1.26 ± 0.13 for \bar{b}_r , 0.931 ± 0.016 for \bar{I}_p and 1.36 ± 0.14 for $\bar{\sigma}_{resid}$. On the other hand, the relative radial symmetry has improved for R , \bar{m} & \bar{I}_p but not for \bar{b}_r and $\bar{\sigma}_{resid}$ due to the additional scattered light. The axial symmetry has improved, giving an average linear coefficient in R which has decreased by a factor of 0.051 ± 0.006 . The more collimated beam and ability to vary ring sizes thus has a drawback of worse beam parameters in general.

So far, a lens with $f_1 = 100\text{ mm}$ has been used to focus the ring. However, similar to focusing Gaussian beams, the focal length may effect the width of the focused ring. Moreover, different focal length lenses result in different extents of collimation. To investigate this effect, the same trap has been set-up with 2 other lenses with $f_1 = 125\text{ mm}$ & $f_1 = 200\text{ mm}$. The results of these traps are shown in fig. 11.

The hollow beam generated with $f_1 = 100\text{ mm}$ can be seen to be the most collimated, having the lowest absolute values for c_+ & c_- . This is in contrast with the expectation of the larger phase for the smaller focal length causing a more diverging beam. This can be explained by the different positions of the image plane w.r.t. the plane of focus. The beam is expected to be the most parallel around the lens focus. However, the optimum ring has been found to lie just before the focus. This is caused due to the fact that the peak intensity is seen to lie at larger radii w.r.t. the rest of the ring profile for the rings closer to the focus. This causes less steep walls, which is why linear coefficients in \bar{m} have the opposite sign to those in R . For the larger focal length lenses, the focus lies further away from this optimum position to the extent that it gives a less axially symmetric beam in R .

For the $f_1 = 100\text{ mm}$ lens, the optimum ring has been found at a distance from the lens of $0.984 \pm 0.017 \times f_1$. For $f_1 = 125\text{ mm}$ it has been found at $0.852 \pm 0.017 \times f_1$. For $f_1 = 200\text{ mm}$ it has been found at $0.840 \pm 0.017 \times f_1$.

For the most diverging beams in sections 3.1 & 3.2, the peak intensity is seen to decrease due to the larger area the light is spread out over. For the least diverging 3 axicon set-ups, the beam is collimated enough that the increase in peak intensity due to the focusing dominates. As the $f_1 = 100\text{ mm}$ trap lies around the focus, we can see that \bar{I}_p lies at a maximum, whereas \bar{I}_p increases with distance for the larger f_1 lenses, due to lying further before the focus as described previously.

The other trap parameters show there may be an optimum focal length given the axicons used, with the $f_1 = 125\text{ mm}$ lens generally providing the best trap parameters.

4 RESULTS OVERVIEW

The results from the analysis of all trap set-ups is shown in fig. 11.

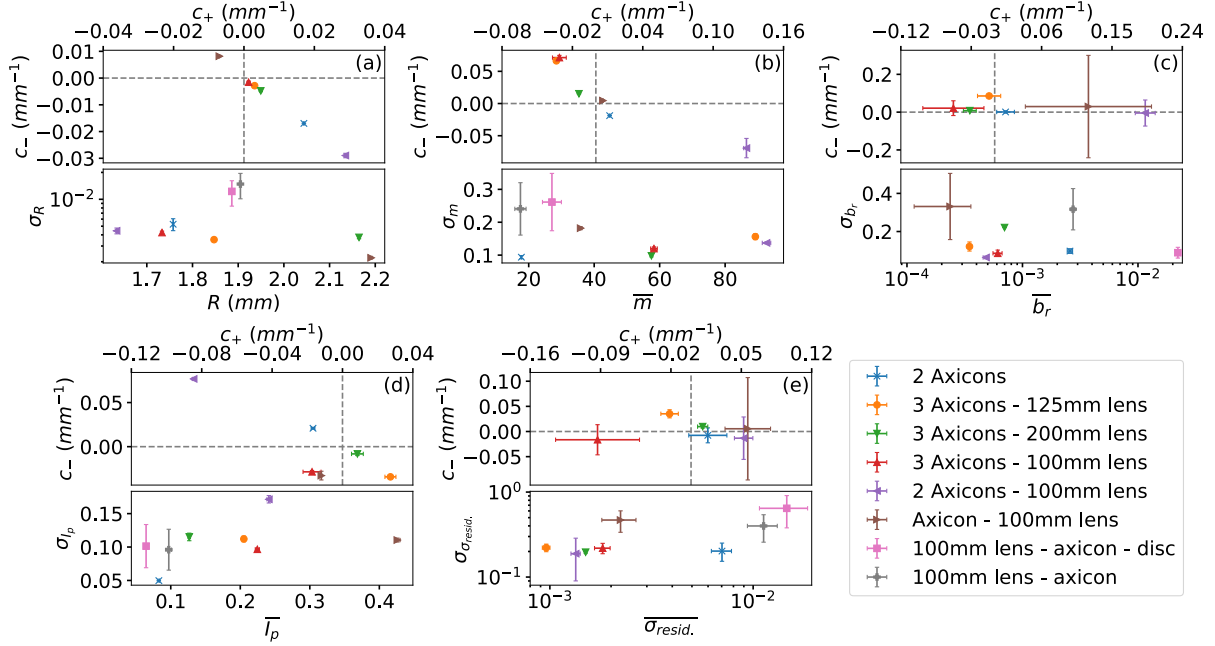


Figure 11: The measured trap parameters of the set-ups described in sections 2.3, 2.4, 3.1, 3.2 & 3.4. (a) On the bottom: the ring radius of the intensity peak, R , plotted with the relative radial standard deviation σ_R in R . This shows the radial symmetry in R . On the top: the relative linear gradients in R w.r.t. propagation distance. c_+ points along the direction of propagation and c_- against, showing the axial symmetry in R . The top/bottom right/left quadrant signifies a parameter minimum/maximun. (b) The same relative parameters as in (a) for the average exponent of the power law fits, \bar{m} , characterising the wall steepness of the trap. (c) The relative parameters for the average power law constant, \bar{b}_r , which is normalised to the peak intensity, \bar{I}_p . This shows the relative trap darkness. (d) The relative parameters for the average peak intensity of the ring, \bar{I}_p , which normalised to the peak intensity of the initial Gaussian beam. (e) The relative parameters of the average standard deviation of the residuals on the power law fit, $\bar{\sigma}_{\text{resid}}$, which is normalised to the peak intensity, \bar{I}_p . This characteres the flatness of the trap.

It should be noted that further investigation may be required in finding the balance between ring size and magnification when reducing the rings to μm scale as is often used for trapping. A larger ring size which is imaged onto a smaller area will have a larger exponent than a smaller ring which is not demagnified at all. However, the demagnification causes the length of the ring that is imaged to be longer, increasing potential axial asymmetry.

5 IMAGE PROCESSING

In order to optimise a box trap and characterise its performance, an image processing programme is required. To that end, a Python programme has been developed as part of this work and is available here: <https://github.com/JochenLangen/trap-analysis.git>.

6 ACKNOWLEDGMENTS

I would like to thank Dr Tobias Franzen for the feedback throughout the project and the guidance in the lab. Additionally, I would like to thank Prof Simon Cornish for his support and feedback through all the project meetings.

7 CONCLUSION

In this work, an overview has been given of the mechanism behind particle trapping using the Jaynes-Cummings model and AC Stark shift. The trap parameters of interest for the use of trapping atoms as well as molecules, which relate to homogeneity and darkness of the trap, have been discussed. This has been turned into a framework of parameters to measure to fully characterise the traps and compare them for the different usage scenarios, which has been achieved using power law fits of different sections of the trap. A theoretical description has been given describing the geometry and phase of light passing through a system of axicons, the element used to generate the hollow beam which is integral to the box trap. From this description, the shape of potential traps can be modelled.

Different arrangements of up to 3 axicons, lenses with focal lengths between 100 mm & 200 mm, obstructing discs and irises have been discussed. Guidance has been given to their set-up and alignment with the results from each configuration having been compared. It can be concluded that the trap consisting of two 2° axicons, one 5° axicon and one 125 mm lens provides the best trap overall. It is one of the most collimated set-ups with one of the steepest walls, darkest centres whilst also having the best flatness. Furthermore, it allows for easy variability by moving the 3rd axicon on a translation stage. The 3rd axicon has been seen to worsen some of the parameters, though, depending on the usage case, the benefit of the variability and collimation can outweigh that. If efficiency of the intensity through-put, cost of optical elements and ease of setting up are a priority, the axicon - lens trap has been found to give the best results.

The Python programme with which these set-ups have been compared has been provided as a tool to align as well as characterise different hollow traps.

References

- [1] Saffman, M. (2016). Quantum computing with atomic qubits and Rydberg Interactions: Progress and challenges. *Journal of Physics B: Atomic, Molecular and Optical Physics*, 49(20), 202001. <https://doi.org/10.1088/0953-4075/49/20/202001>
- [2] Pesce, G., Jones, P. H., Maragò, O. M., & Volpe, G. (2020). Optical tweezers: Theory and practice. *The European Physical Journal Plus*, 135(12). <https://doi.org/10.1140/epjp/s13360-020-00843-5>
- [3] Dalfovo, F., Giorgini, S., Pitaevskii, L. P., & Stringari, S. (1999). Theory of bose-einstein condensation in trapped gases. *Reviews of Modern Physics*, 71(3), 463–512. <https://doi.org/10.1103/revmodphys.71.463>
- [4] Navon, N., Smith, R. P., & Hadzibabic, Z. (2021). Quantum gases in optical boxes. *Nature Physics*, 17(12), 1334–1341. <https://doi.org/10.1038/s41567-021-01403-z>

- [5] Gaunt, A. L., Schmidutz, T. F., Gotlibovych, I., Smith, R. P., & Hadzibabic, Z. (2013a). Bose-Einstein condensation of atoms in a uniform potential. *Physical Review Letters*, 110(20). <https://doi.org/10.1103/physrevlett.110.200406>
- [6] Schmidutz, T. F., Gotlibovych, I., Gaunt, A. L., Smith, R. P., Navon, N., & Hadzibabic, Z. (2014a). Quantum Joule-Thomson effect in a saturated homogeneous Bose Gas. *Physical Review Letters*, 112(4). <https://doi.org/10.1103/physrevlett.112.040403>
- [7] Hueck, K., Luick, N., Sobirey, L., Siegl, J., Lompe, T., & Moritz, H. (2018). Two-dimensional homogeneous Fermi gases. *Physical Review Letters*, 120(6). <https://doi.org/10.1103/physrevlett.120.060402>
- [8] Mukherjee, B., Yan, Z., Patel, P. B., Hadzibabic, Z., Yefsah, T., Struck, J., & Zwierlein, M. W. (2017). Homogeneous atomic fermi gases. *Physical Review Letters*, 118(12). <https://doi.org/10.1103/physrevlett.118.123401>
- [9] Chomaz, L., Corman, L., Bienaimé, T., Desbuquois, R., Weitenberg, C., Nascimbène, S., Beugnon, J., & Dalibard, J. (2015b). Emergence of coherence via transverse condensation in a uniform quasi-two-dimensional Bose Gas. *Nature Communications*, 6(1). <https://doi.org/10.1038/ncomms7162>
- [10] Christianen, A., Zwierlein, M. W., Groenenboom, G. C., & Karman, T. (2019). Photoinduced two-body loss of ultracold molecules. *Physical Review Letters*, 123(12). <https://doi.org/10.1103/physrevlett.123.123402>
- [11] Mayle, M., Quéméner, G., Ruzic, B. P., & Bohn, J. L. (2013). Scattering of ultracold molecules in the highly resonant regime. *Physical Review A*, 87(1). <https://doi.org/10.1103/physreva.87.012709>
- [12] Bause, R., Schindewolf, A., Tao, R., Duda, M., Chen, X.-Y., Quéméner, G., Karman, T., Christianen, A., Bloch, I., & Luo, X.-Y. (2021). Collisions of ultracold molecules in bright and dark optical dipole traps. *Physical Review Research*, 3(3). <https://doi.org/10.1103/physrevresearch.3.033013>
- [13] Gregory, P. D., Blackmore, J. A., Bromley, S. L., & Cornish, S. L. (2020). Loss of Ultracold $^{87}\text{Rb}^{133}\text{Cs}$ Molecules via Optical Excitation of Long-Lived Two-Body Collision Complexes. *Physical Review Letters*, 124(16). <https://doi.org/10.1103/physrevlett.124.163402>
- [14] Cornish, S. L., & Hutson, J. M. (2022). Toward a coherent ultracold chemistry. *Science*, 375(6584), 975–976. <https://doi.org/10.1126/science.abn1053>
- [15] Gerry, C. & Knight, P. L. (2005). *Introductory Quantum Optics*. Cambridge University Press.
- [16] Foot, C. J. (2012). *Atomic physics*. Oxford University Press.
- [17] Grimm, R., Weidemüller, M., & Ovchinnikov, Y. B. (2000). Optical dipole traps for neutral atoms. *Advances In Atomic, Molecular, and Optical Physics*, 95–170. [https://doi.org/10.1016/s1049-250x\(08\)60186-x](https://doi.org/10.1016/s1049-250x(08)60186-x)
- [18] Manek, I., Ovchinnikov, Y. B. & Grimm, R. (1998). Generation of a hollow laser beam for atom trapping using an axicon. *Optics Communications*, 147(1-3), 67–70. [https://doi.org/10.1016/s0030-4018\(97\)00645-7](https://doi.org/10.1016/s0030-4018(97)00645-7)
- [19] Zhai, Z., Cheng, Z., Lv, Q. & Wang, X. (2020). Tunable Axicons generated by spatial light modulator with high-level phase computer-generated holograms. *Applied Sciences*, 10(15), 5127. <https://doi.org/10.3390/app10155127>
- [20] de Angelis, M., Cacciapuoti, L., Pierattini, G., & Tino, G. M. (2003). Axially symmetric hollow beams using refractive conical lenses. *Optics and Lasers in Engineering*, 39(3), 283–291. [https://doi.org/10.1016/s0143-8166\(01\)00117-8](https://doi.org/10.1016/s0143-8166(01)00117-8)
- [21] Wei, M.-D., Shiao, W.-L., & Lin, Y.-T. (2005). Adjustable generation of bottle and hollow beams using an axicon. *Optics Communications*, 248(1-3), 7–14. <https://doi.org/10.1016/j.optcom.2004.11.092>
- [22] Khonina, S. N., Porfirev, A. P., Volotovskiy, S. G., Ustinov, A. V., Fomchenkov, S. A., Pavelyev, V. S., Schröter, S., & Duparré, M. (2021). Generation of multiple vector optical bottle beams. *Photonics*, 8(6), 218. <https://doi.org/10.3390/photonics8060218>
- [23] Khilo, N. A., Ropot, P. I., Piatrou, P. K., & Belyi, V. N. (2021). Bessel-like light beams formed by the two-component scheme consisting of axicon and spherical lens. *Optics Communications*, 483, 126666. <https://doi.org/10.1016/j.optcom.2020.126666>
- [24] Lei, M., & Yao, B. (2004). Characteristics of beam profile of gaussian beam passing through an axicon. *Optics Communications*, 239(4-6), 367–372. <https://doi.org/10.1016/j.optcom.2004.05.048>

- [25] Nguyen, H. D., Sedao, X., Mauclair, C., Bidron, G., Faure, N., Moreno, E., Colombier, J.-P., & Stoian, R. (2020a). Non-diffractive bessel beams for ultrafast laser scanning platform and proof-of-concept side-wall polishing of additively manufactured parts. *Micromachines*, 11(11), 974. <https://doi.org/10.3390/mi11110974>
- [26] Hughes, I. & Adams, C. (2019). From Fourier to Fresnel; New York; Oxford University Press.
- [27] Vdovin, G. V., Van Brug, H. H., & Van Goor, F. A. (n.d.). LightPipes for PythonVersion (2.1.3). Retrieved January 8, 2023, from <https://opticspy.github.io/lightpipes/>
- [28] Malitson, I. H. (1965a). Interspecimen comparison of the refractive index of fused silica*,†. *Journal of the Optical Society of America*, 55(10), 1205–1208. <https://doi.org/10.1364/josa.55.001205>
- [29] Kubitscheck, U. & Heintzmann, R. (2017). Appendix B: Practical Guide to Optical Alignment. In *Fluorescence microscopy: From principles to biological applications* (2nd ed., pp. 463–471). Wiley-VCH.
- [30] Freedman, D. & Diaconis, P. (1981). On the histogram as a density estimator:L 2 theory. *Zeitschrift Für Wahrscheinlichkeitstheorie Und Verwandte Gebiete*, 57(4), 453–476. <https://doi.org/10.1007/bf01025868>
- [31] Hughes, I. & Hase, T. (2010). Measurements and their uncertainties: A practical guide to modern error analysis. Oxford University Press.

8 Appendix

8.1 Camera linearity

The linearity of the camera has been investigated to ensure the different images can be scaled and combined. The results are shown in fig. 12.

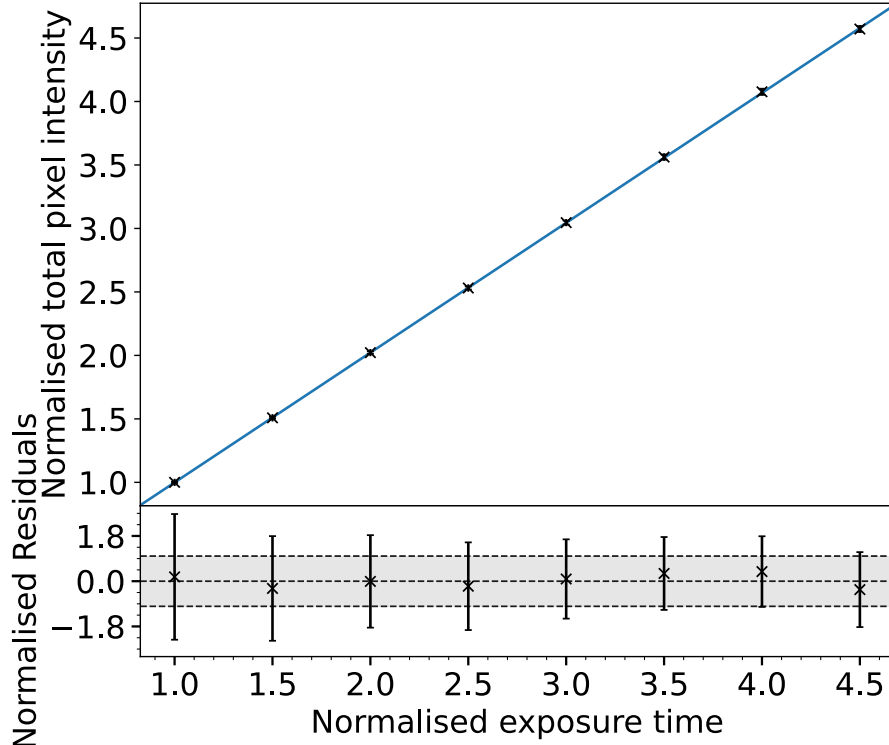


Figure 12: A linear fit to the average pixel intensity against the exposure time. The images picture the same surface. The intensity and exposure times have been normalised by their lowest values.

8.2 Gaussian noise

The light intensity, coming from a coherent photon state, is described by Poissonian statistics [15]. The photon energy is $E_\gamma = 2.33 \text{ eV}$ for $\lambda = 532 \text{ nm}$ [15]. For the axicon - lens set-up the energy in the trap centre can be estimated as:

$$E_{\text{centre}} = t_{\text{exp}} \cdot P_{\text{total}} \cdot \frac{I_{\text{centre}} V_{\text{centre}}}{I_{\text{peak}} V_{\text{peak}}} \approx t_{\text{exp}} \cdot P \cdot \frac{I_{\text{centre}} (R_{\text{outer}}^2 - R_{\text{inner}}^2)}{I_{\text{peak}} R_{\text{inner}}^2} \approx 2 \cdot 10^7 E_\gamma, \quad (29)$$

where t_{exp} is the exposure time of $52.03 \mu\text{s}$, P_{total} the total power of $167 \cdot 10^{-6} \text{ W}$, I_{centre} is the intensity in the centre, which is 10^{-4} for $I_{\text{peak}} = 1$ and the inner and outer radii, R_{inner} & R_{outer} , are determined from fig. 4 (b) & (c). Therefore, the large number of photons in this experiment means a Poissonian distribution is approximately Gaussian [31]. This has been determined for the set-up in fig. 4, though the same holds for the other set-ups.